Journal of The Electrochemical Society, **153** (7) A1317-A1324 (2006)
0013-4651/2006/153(7)/A1317/8/$20.00 © The Electrochemical Society

Investigation of Pseudocapacitive Charge-Storage Reaction of $MnO_2 \cdot nH_2O$ Supercapacitors in Aqueous Electrolytes

Shin-Liang Kuo and Nae-Lih Wu*,z

Department of Chemical Engineering, National Taiwan University, Taipei, Taiwan 106

Pseudocapacitive charge-storage reaction of $MnO_2 \cdot nH_2O$ in several aqueous alkali and alkaline salts solutions, including LiCl, NaCl, KCl, CsCl, and $CaCl_2$, has been studied on fine-grained $MnO_2 \cdot nH_2O$ thin films and particles which possess the ε-MnO_2-type crystal structure. In situ synchrotron X-ray diffraction analysis shows that charge transfer at Mn sites upon reduction/oxidation of $MnO_2 \cdot nH_2O$ is balanced by bulk insertion/extraction of the solution cations into/from the oxide structure, which causes reversible expansion and shrinkage in lattice spacing of the oxide during charge/discharge cycles. Electrochemical quartz-crystal microbalance and X-ray photoelectron spectroscopy data further indicate that H_3O^+ plays the predominant (>60%) role in all cases, while the extent of participation of alkali cations first decreases and then increases with ionic size. The charge-storage reaction can be summarized as: $Mn(IV)O_2 \cdot nH_2O + \delta e^- + \delta(1-f)H_3O^+ + \delta f M^+ \rightleftharpoons (H_3O)_{\delta(1-f)}M_{\delta f}[Mn(III)_\delta Mn(IV)_{1-\delta}]O_2 \cdot nH_2O$, where M^+ is alkali cation.
 [DOI: 10.1149/1.2197667]

Manuscript submitted January 5, 2006; revised manuscript received March 10, 2006. Available electronically May 9, 2006.

Depending on the charge-storage mechanism, supercapacitors can be divided into two categories. The first category is electric double layer capacitor (EDLC), of which capacitance arises from potential dependence of the surface density of charges stored electrostatically at the interfaces of capacitor electrodes.[1-4] The second category is the so-called pseudocapacitor, which involves faradaic reactions but behaves like a capacitor rather than a galvanic cell.[5-16] The pseudocapacitors typically exhibit a capacitance per unit surface area of the electrode material that is up to 10 times that of the EDLCs.

One promising pseudocapacitive material is hydrated amorphous or nanocrystalline manganese oxide, $MnO_2 \cdot nH_2O$.[10,17-20] This material has exhibited capacitances exceeding 200 F/g in solutions of several alkali salts, such as LiCl, NaCl, and KCl. Although there has been a general consensus that the charge storage involves electron transfer at Mn sites, the interfacial reaction mechanism that balances the charge transfer remains unclear. Lee et al.[10,17] suggested that for both $MnO_2 \cdot nH_2O$ and $K_xMnO_2 \cdot nH_2O$ supercapacitors with aqueous KCl electrolyte solution, charge transfer at Mn sites is balanced by the chemisorption/desorption of K^+. Pang et al.[18] proposed that the pseudocapacitance involves "intercalation" or insertion of protons within the near-surface region, which generally can be expressed as

$$MnOOH_\delta + \lambda H^+ + \lambda e^- \rightleftharpoons MnO_{2-\lambda}(OH)_{\delta+\lambda} \quad [1]$$

Toupin et al.[19] performed ex situ X-ray photoelectron spectroscopy (XPS) measurement on a $K_xMnO_2 \cdot nH_2O$ electrode subjected to charge/discharge in NaCl aqueous solution. Their results showed that the valence of Mn varied between +4 and +3 and that the Na content, as determined by X-ray photoelectron spectroscopy (XPS), was far less than would account for the total amount of charge transferred. Their results may suggest that a cation(s) other than Na^+ is operative for balancing the valence variation of Mn ions.

In this work, the interfacial reaction mechanism leading to the pseudocapacitance of $MnO_2 \cdot nH_2O$ in several aqueous alkali and alkaline salts solutions, including $NaCl_{(aq)}$, $KCl_{(aq)}$, $LiCl_{(aq)}$, $CsCl_{(aq)}$, and $CaCl_{2(aq)}$, was investigated mainly by using electrochemical quartz-crystal microbalance (EQCM) analysis, in situ synchrotron X-ray diffraction (XRD), and XPS. In brief, the results clearly show that bulk insertion/extraction of H_3O^+ into/from the structure of $MnO_2 \cdot nH_2O$ plays the predominant role in all cases.

Experimental

Two types, including thin-film and particle, of $MnO_2 \cdot nH_2O$ samples have been synthesized for different analyses. $MnO_2 \cdot nH_2O$ thin films were deposited onto the gold working electrode in the EQCM cell (CHI 405a, CH Instrument) by an anodic deposition process according to Ref. 20. The electroplating solution is 0.25 M $MnSO_4$ solution with pH 5.0. The deposition was performed under a constant potential of 0.9 V with respect to Ag/AgCl/ saturated $KCl_{(aq)}$ [EG&G, potential 197 mV vs a normal hydrogen reference electrode (NHE) at 25°C] with a total passed charge of 0.2 C/cm^2. The amount of deposit was simultaneously monitored by the quartz-crystal microbalance. After deposition, the electrode was washed with deionized water prior to subsequent analyses.

$MnO_2 \cdot nH_2O$ particles were precipitated by mixing 0.15 M $KMnO_4$ and 0.15 M $MnSO_4$ aqueous solutions with a Mn(VII)/Mn(II) molar ratio of 2:3 at 25°C. After a thorough wash with deionized water, the particles were finally heated at 200°C for 1 h in air.

Synchrotron XRD and X-ray absorption near-edge structure (XANES) analyses used the electrodes made of the mixture of the $MnO_2 \cdot nH_2O$ particles and conductive carbon black (VULCAN XC72, Cabot Corp., USA) with a weight ratio of 8:2. Poly(tetrafluoroethylene) (PTFE) (5 wt%) was used as the binder and Ti mesh was used as the current collector. The electrodes were finally dried at 120°C for 6 h in vacuum. Analyses were conducted with the beam line 01-C2 (for XRD) and 17-C1 (for XANES) facilities of the National Synchrotron Radiation Research Center (NSRRC) in Taiwan. The synchrotron XRD instrument setup is shown in Fig. 1a, and the construction of the electrochemical cell for both in situ studies is illustrated in Fig. 1b. The main body of the cell was made of acrylics, and the two sides of the cell were perforated and then sealed with Kapton foils in order to allow the probing beam to pass through the cell. The X-ray wavelength of either 0.0775 or 0.09537 nm was used. The patterns were acquired during the course of a cyclic voltammetric (CV) scan running at a scan rate of 0.2 mV/s between 0.0 and 1.0 V (vs Ag/AgCl), and they were recorded by a curved translating imaging plate (Fuji BAS2500) with the sample-to-film distance of 280 mm. Two-dimensional data were converted using the FIT2D program. For the in situ XANES study, CV ran at a scan rate of 0.2 mV/s, and the potential was stopped at each of the selected values for 10 min for data collection.

EQCM analysis measures the frequency difference between the working crystal and the reference crystal. The resonant frequency of the fundamental mode of the reference crystal (f_o) is 8.0 MHz. The correlation between mass change (Δm) and frequency variation (Δf) was calculated based on the Sauerbrey equation

$$\Delta f = -2f_o^2 \Delta M / A(\mu\rho)^{0.5} \quad [2]$$

where Δf is in hertz, ΔM is in grams, A is the area of the gold working electrode (0.196 cm^2), μ is the shear parameter of quartz

* E-mail: Electrochemical Society Active Member.
z E-mail: nlw001@ntu.edu.tw

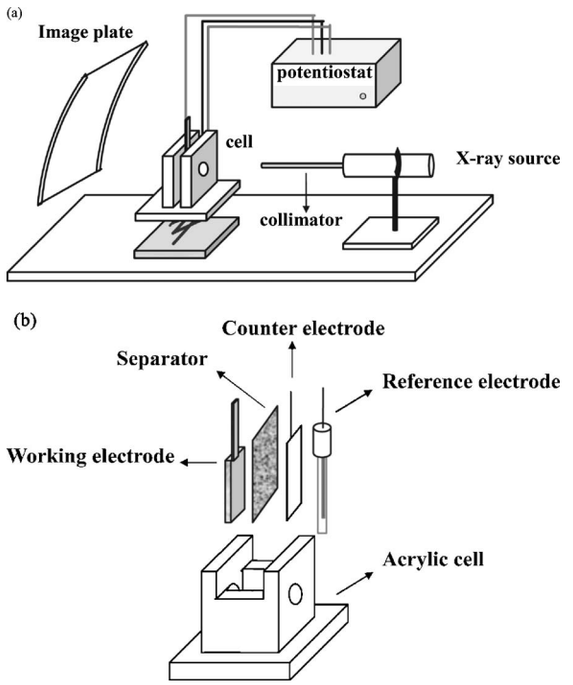

Figure 1. (a) Instrument setup for the in situ synchrotron XRD analysis and (b) constructin of the electrochemical cell.

$(2.947 \times 10^{11}$ g/cm $s^2)$, and ρ is the density of quartz $(2.684$ g/$cm^3)$. Substitution of all the parameters into Eq. 2 shows that a frequency variation of +1 Hz corresponds to a mass change of −1.4 ng. In a typical run, the potential of the oxide-coated working electrode was cycled at a constant scan rate in a three electrode configuration which comprises a platinum counter electrode and a Ag/AgCl reference electrode, and the current and quartz frequency were simultaneously recorded. The aqueous electrolyte solutions for this study include 1 M solutions of LiCl, NaCl, KCl, CsCl, and $CaCl_2$. The specific capacitance, C_s, was calculated by

$$C_s = I/s/w \qquad [3]$$

where I is the average of the anodic and cathodic currents measured at the middle of the potential window, s is the potential scan rate, and w the mass of the oxide thin film.

The morphologies of the film and particle samples were examined by scanning electron microscopy (SEM; LEO 1530). XPS analysis was carried out on a spectrometer (MT 500, VG Microtech) equipped with a Mg (Kα) X-ray source. The C 1 s peak at 248.8 eV was used as the reference for calibration. To prepare for the XPS analysis, the film electrodes which were removed out of electrolyte solutions were first thoroughly rinsed, then sandwiched between two filter papers to remove a major portion of the residue solution, and finally dried at 50°C in air.

Results

Electroplating of MnO_2.— Figure 2 shows the current and mass change during the electroplating process. It was found that upon imposing a step potential, the current started very high and then quickly dropped to a fairly constant value of ~0.1 mA. Concurrently, the mass of the electrode first increased with high rates and then linearly with time. Throughout the entire deposition period, the mass-to-charge ratio (MCR), is defined as

$$MCR \equiv dM/(dQ/-96{,}500) \qquad [4]$$

where dM is the differential mass change of the electrode (g) and dQ, the differential charge change (coulomb), remains fairly constant at −46.70 g/mol e^-. MCR has the physical meaning of the mass gain (or loss) caused by reduction (or oxidation) by 1 mole of electron (e^-). If the ratio has a negative sign, species is added onto the working electrode upon oxidation. This is exactly the case for anodic plating.

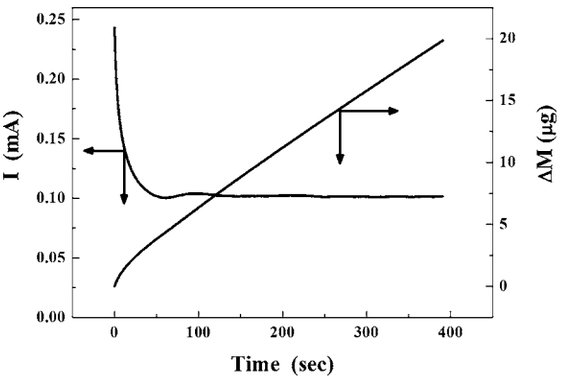

Figure 2. Current (I) and accumulated mass variation (ΔM) during the anodic plating process of MnO_2 at potential of 0.9 V with a total charge of 0.2 C/cm^2.

The anodic plating reaction in the present study, which uses Mn(II) salt as the starting reagent, can nominally be expressed as

$$Mn^{+2} + 2H_2O \leftrightarrow MnO_2 + 4H^+ + 2e^- \qquad [5]$$

which has a theoretical MCR of −43.47. The magnitude of the measured MCR (46.7) is close to the theoretical value. This suggests that the plating process involves a two-electron transfer mechanism as written. The difference between the ratios may also suggest that the plated MnO_2 film is not stoichiometric but has a larger formula weight than MnO_2. This difference is believed to arise from incorporation of water molecules into the oxide film during plating. Accordingly, the measured MCR corresponds to a chemical formula of $MnO_2{\cdot}0.36\ H_2O$.

Conventional powder XRD of the film electrode did not detect any reflection other than those of the substrate (Au). Further attempts to analyze the crystal structure of the oxide film were carried out by peeling off the film from the Au substrate with Scotch tape and then subjecting the film-on-tape sample to synchrotron XRD under transmission mode. As shown in Fig. 3 (curve a), the oxide

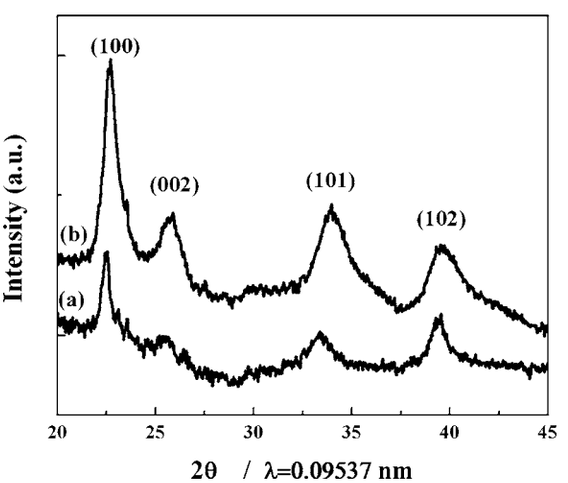

Figure 3. Synchrotron XRD patterns for (a) electroplated thin film and (b) precipitated particles of $MnO_2{\cdot}nH_2O$. The (h k l) indexation is based on ε -MnO_2 structure, Ref. 22.

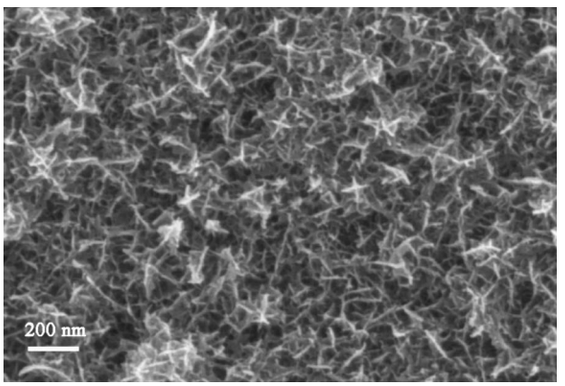

Figure 4. SEM micrograph of the electroplated $MnO_2 \cdot nH_2O$ film electrode.

film exhibited broad reflection peaks which can be indexed with the structure of ε-MnO_2,[21,22] which has a hexagonal lattice, with parameters a = 2.822 nm and c = 4.528 nm. The observed lattice parameters are slightly larger than those reported in the literature,[21] and the difference may be ascribed to poor crystallinity and to the presence of water molecules within the structure of the present material. The Scherrer crystallite size is 6.0 nm, as calculated based on the linewidth of the (100) peak. SEM examination indicated that the oxide film has a porous structure (Fig. 4).

EQCM study.— Figure 5a shows the CVs of the film electrode in 1 M NaCl aqueous solution. Analyses using the thin-film electrode were limited by a cathodic potential end of 0.5 V, below which the oxide films tended to detach from the Au substrate in some cases. The detachment presumably results from volume (lattice) expansion of the oxide film during reduction, which, as described later, was evidenced by synchrotron XRD. As shown in Fig. 5a, the voltammograms showed an almost ideal rectangular profile, consistent with the literature using the powder electrodes. The line profile is quite different from that exhibited by $RuO_2 \cdot nH_2O$ electrode in sulfuric acid solution, which typically shows profiles containing multiple redox humps.[23] The specific capacitances are 224 and 199 F/g at 10 and 50 mV/s, respectively (Table I). Figure 5b shows the accumulative charge (ΔQ; "–" sign for reduction) curves for different scan rates, which were calculated by integrating the current data. The closed-loop nature of the ΔQ curves indicates that the charge transferred during the cathodic scan is totally released during the anodic scan. The slight separation of the anodic and cathodic branches of the ΔQ loops results from the delay in current response on voltage reversal at the potential ends.

Figure 5c plots the accumulated mass change (ΔM) vs charge (ΔQ). First, all the curves are closed-loop in nature, suggesting that all the species incorporated into the electrode were eventually released from electrode after every CV cycle. Second, the curves of different scan rates overlapped with one another, suggesting that neither the operating species nor the reaction mechanism is affected by the scan rate. Third, all the curves are essentially linear lines with a mean MCR (as defined by Eq. 4) of 18.7 (±0.7) g/mol e^-. The simple linearity of the curves indicates an only one-stage redox reaction occurring. This is in contrast with the case of $RuO_2 \cdot nH_2O$, which exhibited regions of different MCRs due to the occurrence of multiple-stage redox reactions.[23] Furthermore, the positive sign of the MCR implies a cation-, but not anion-, operating redox reaction. It is noted that the MCR value (18.7 g/mol e^-) is nothing close to the atomic weight of either H (1.0 g/mol) or Na (23 g/mol).

The same studies as described above have also been carried out in LiCl, KCl, CsCl, and $CaCl_2$ solutions. Figure 6a shows the voltammograms at the scan rate of 50 mV/s for these solutions. In all cases, the CV curves again exhibit ideal rectangular profiles. As listed in Table I, the specific capacitance varied slightly among different electrolytes. High capacitances were also observed even for the Ca^{+2} electrolyte solution. The corresponding mass-vs-charge plots of these solutions are shown in Fig. 6b. Linear correlation holds for all the solutions. LiCl, KCl, and $CaCl_2$ solutions give similar MCRs, within the range between 16.2 and 21.6. In contrast, CsCl solution gives a distinctly higher MCR, 59.9 (Table II).

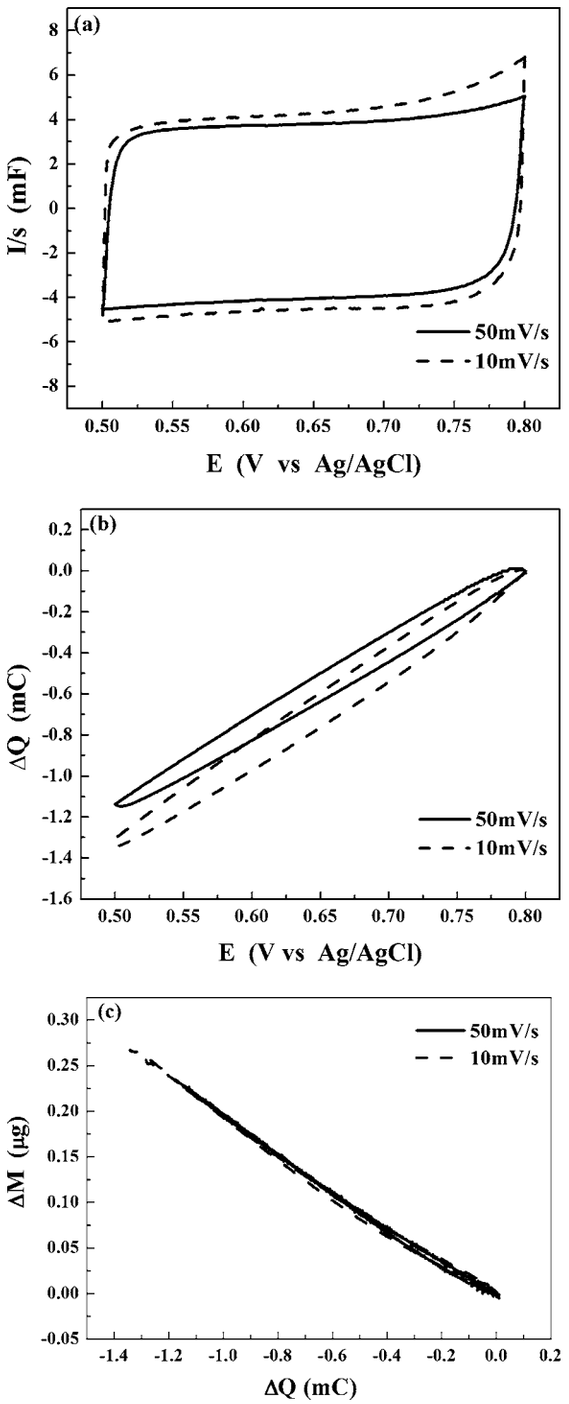

Figure 5. (a) CVs, where I is current and s the potential scan rate, (b) ΔQ (accumulated charge) plots, and (c) ΔM (accumulated mass variation) vs ΔQ plots of $MnO_2 \cdot nH_2O$ film electrode in 1 M $NaCl_{(aq)}$ at different potential scan rates.

Table I. Specific capacitances of the plated $MnO_2 \cdot nH_2O$ film in different electrolytes.

	Scan rate	
	50 mV/s	10 mV/s
Electrolyte	Specific capacitance (F/g)	
LiCl	184	204
NaCl	199	224
KCl	183	204
CsCl	161	183
$CaCl_2$	149	218

XPS analysis.— To prepare for the XPS analysis, the film electrodes were respectively cycled in different solutions between 0.8 and 0.5 V ten times and then stopped at the end of the cathodic scan, i.e., 0.5 V, for 5 min. At the fresh surface of the oxide films, XPS detected a Mn $2p_{3/2}$ peak at the binding energy (BE) of 642.9 eV (solid line in Fig. 7a). However, the peak was found to shift to a lower BE of 641.1 eV after the surface was etched for 5 min and remained unchanged with further etching up to 10 min. (The total etched distance was estimated to be less than 10 nm.) The same results were observed for the electrodes cycled in all the electrolyte solutions employed. The BE of 642.9 eV is best accounted for by Mn(IV) according to Ref. 24. The shift to lower BE after etching suggested that the Mn species located below the film surface has a mean valence less than +4. The BE of Mn $2p_{3/2}$ for the interior Mn ions is 641.1 eV (Fig. 7a), which coincides with that reported for $Mn(III)_2O_3$.[24] The results indicate that the Mn ions at the grain surface are susceptible to oxidation by even a rather mild drying process, such as heating at 50°C in air. Direct evidence to valence variation of Mn ions upon charge/discharge is given by in situ XANES analysis.

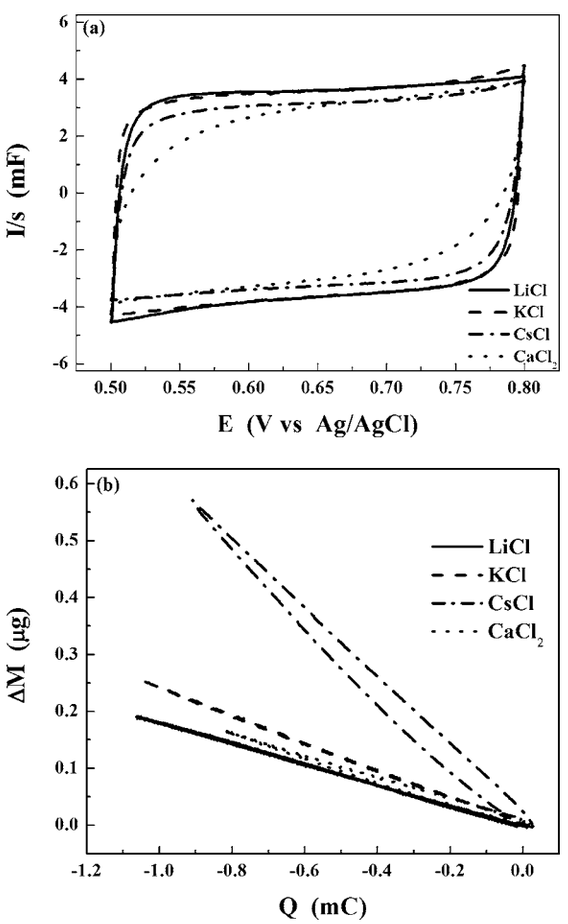

Figure 6. (a) CVs, where I is current and s the potential scan rate, and (b) ΔM (accumulated mass variation) vs ΔQ (accumulated charge) plots of $MnO_2 \cdot nH_2O$ film electrodes in different electrolytes. The potential scan rate is 50 mV/s.

Table II. EQCM data of the electroplated $MnO_2 \cdot nH_2O$ film electrodes.

Electrolyte	EW of cation[a] (g/mol)	MCR[b] (g/mol e^-)	σ of MCR[c] (g/mol e^-)	f[d] (%)
NaCl	23	18.7	0.7	<5
LiCl	7	16.2	1.8	23.3
KCl	39	21.6	2.6	13.0
CsCl	133	59.9	4.6	35.8
$CaCl_2$	20	19.8	0.7	UD[e]

[a] EW: equivalent weight.
[b] MCR: mass-to-charge ratio.
[c] σ of MCR: the standard deviation of the mass-to-charge ratio.
[d] f: the contribution, in molar fraction, of alkali cation in inserting cation flux.
[e] UD: unable to determine.

XPS did not detect any Li signal on the film electrode reduced in LiCl solution. However, because the XPS atomic sensitivity factor for Li(1s), 0.02, is very small, the data cannot give unequivocal evidence to the presence/absence of Li in the reduced film electrode. Figure 7b-e shows the XPS spectra associated with the other cations of the electrolytes employed. The intensities of all the spectra have been normalized to have the same intensity for the Mn $2p_{3/2}$ signal. For the electrode reduced in NaCl solution, the XPS analysis also did not detect Na, either with or without etching (Fig. 7b). The atomic sensitivity factor for Na is 2.3, and it can readily be detected even with a molar fraction of 1%. The absence of Na signal in this case did indicate that Na^+ was not incorporated into the oxide film during reduction. The data also serve to illustrate that the residue electrolyte salts can be efficiently removed from the electrode surface by the rinsing procedure adopted, and they do not impose controversy in data interpretation. In contrast to NaCl and LiCl solutions, for electrodes reduced in other electrolyte solutions, including KCl, CsCl, and $CaCl_2$ solutions, the XPS peaks of the corresponding cations were vividly detected (Fig. 7c-e).

In situ synchrotron XRD analysis.— The synchrotron XRD pattern of the $MnO_2 \cdot nH_2O$ particles is shown in Fig. 3 (curve b). The pattern can also be indexed with the ε-MnO_2 structure[21,22] with a = 2.797 nm and c = 4.419 nm. That is, the particles basically have the same lattice structure as the electroplated films, except that the former has smaller lattice parameters, presumably because of different water contents. The pattern, however, is distinctly different from that shown in Ref. 25, which was assigned to the α-MnO_2 structure.

Under CV analysis, the particle electrodes exhibited rectangular current profiles (Fig. 8) of the same characteristics as those of the film electrodes. Particularly, there are also no redox humps throughout the scan potential range (0.0–1.0 V). The great similarities in oxide crystal structure and CV response between the powder and thin-film electrodes lead us to believe that the same mechanism would take place for both of them and their data are complementary to each other.

For in situ synchrotron XRD patterns, the reflections of the Ti current collector are taken as the internal standards. In all the electrolyte solutions employed, the peaks of the $MnO_2 \cdot nH_2O$ particles were clearly seen to shift back and forth upon CV cycling. Two examples, those for the NaCl and KCl solutions, are shown in Fig. 9. In both cases, the (100) peak of the $MnO_2 \cdot nH_2O$ particles was shown to shift toward a lower angle during the cathodic scan, sug-

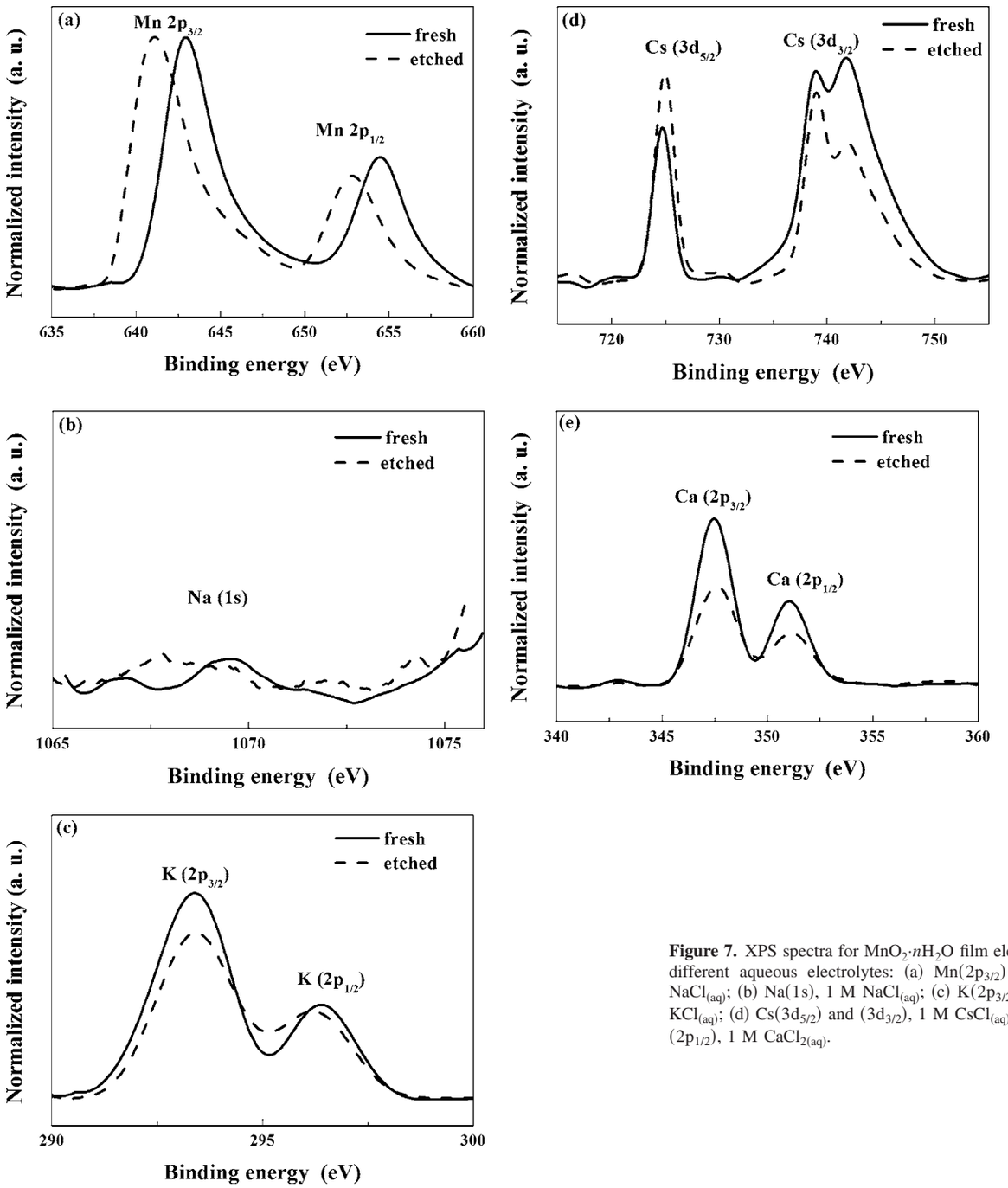

Figure 7. XPS spectra for $MnO_2{\cdot}nH_2O$ film electrodes reduced in different aqueous electrolytes: (a) Mn($2p_{3/2}$) and ($2p_{1/2}$), 1 M $NaCl_{(aq)}$; (b) Na(1s), 1 M $NaCl_{(aq)}$; (c) K($2p_{3/2}$) and ($2p_{1/2}$), 1 M $KCl_{(aq)}$; (d) Cs($3d_{5/2}$) and ($3d_{3/2}$), 1 M $CsCl_{(aq)}$; (e) Ca($2p_{3/2}$) and ($2p_{1/2}$), 1 M $CaCl_{2(aq)}$.

gesting lattice expansion, and then back to the original positions during the anodic scan. The structural variation is completely reversible. The extent of lattice expansion of this reflection is ~10% per mol of e^- transferred for both solutions. The observed lattice expansion indicates that pseudocapacitance of $MnO_2{\cdot}nH_2O$ involves "intercalation" or insertion of cations into the bulk of the oxide structure, but not merely surface adsorption.

XANES analysis.— Figure 10a shows the Mn K-edge XANES spectra of the $MnO_2{\cdot}nH_2O$ particle electrode recorded along the reduction phase of a CV scan from 1.0 to 0.0 V (vs Ag/AgCl), while the first derivative of these spectra are displayed in Fig. 10b. The spectrum of crystalline β-MnO_2 is also plotted for comparison. The line profiles of the XANES spectra taken at different potentials are similar, and they are characterized by features which can be divided among a pre-edge range A showing two weak broad peaks at 6538–6545 eV, a main edge range B having one inflection point, and resonance peak ranges C and D.[26-28] The pre-edge range A is ascribed[26] to 1 s → 3d transitions, which has been observed with weak intensity for octahedral coordination and strong intensity for tetrahedral coordination. Hence, the experimental spectra (Fig. 10a) confirm the octahedral coordination of Mn in $MnO_2{\cdot}nH_2O$ particles.

The main absorption range B can be assigned[26] to the transition from Mn 1 s to p-like states of t_{1u} symmetry. The associated edge energy is conventionally taken as the energy of the first derivative peak (Fig. 10b), which corresponds to the inflection point of range B in the XANES spectra. The edge energy is known to increase with

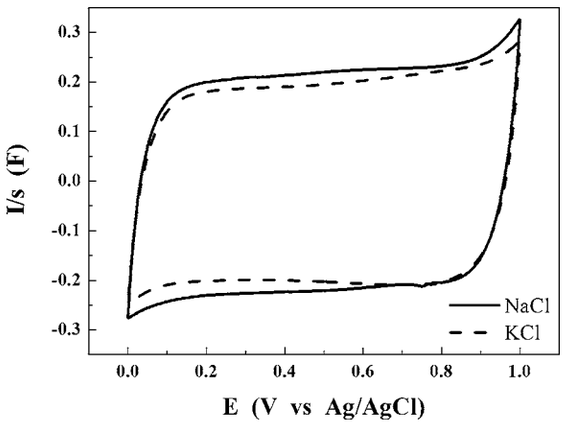

Figure 8. CVs of the powder electrodes cycled at 1 M $NaCl_{(aq)}$ and 1 M $KCl_{(aq)}$, respectively, with potential scan rate of 20 mV/s.

increasing Mn valence for Mn oxides.[26-28] As shown in Fig. 10b, the main absorption edge (B) progressively shifted to lower energies when the potential was reduced from 1.0 to 0.0 V, giving direct evidence to the reduction of Mn ions. It is also noticed that the main absorption edges of all $MnO_2{\cdot}nH_2O$ samples are located at lower energies than that of crystalline β-MnO_2. Hence, the average Mn valence in $MnO_2{\cdot}nH_2O$ particles is less than +4 at all potentials.

Mechanism.— Pseudocapacitance of $MnO_2{\cdot}nH_2O$ in alkali salt solutions has been attributed to either chemisorption of alkali cation or protonation reaction, balancing valence variation at the Mn sites. The former is expected to give a mass to charge ratio (MCR) equal to the equivalent weight of the alkali ion, while the later should give an MCR of +1. As shown in Table II, none of the measured MCRs matches the equivalent weight of either H^+ or alkali ions.

For NaCl solution, XPS did not detect Na in the reduced $MnO_2{\cdot}nH_2O$ electrode. This result is consistent to a large extent with Bélanger et al.,[19] who have shown in a similar experiment that the Na content is far less than what is to account for the total amount of charge transferred. The measured MCR, 18.7 for charge/discharge in NaCl, can be considered equal to the equivalent weight (19.0) of oxonium, H_3O^+, within experimental error. In fact, the MCRs for LiCl, KCl, and $CaCl_2$ solutions, which are between 16.2 and 21.6, are also close to this value. These results lead us to propose that the pseudocapacitance of $MnO_2{\cdot}nH_2O$ in NaCl solution involves almost exclusively the insertion/extraction of H_3O^+ into/from the oxide structure, is accompanied by charge transfer at the Mn sites. The oxide lattice expansion upon reduction, as detected by synchrotron XRD, indicates that the reaction involves not merely surface adsorption, but bulk insertion of cations into the Mn oxide lattice. The size of H_3O^+, as in contrast with that of H^+ alone, is reasonable to account for the observed extent of the lattice expansion (~10% per mole of e^- transferred). For comparison, thermal decomposition of layered $K_xMnO_{2+\delta}{\cdot}nH_2O$ between 300 and 800°C has been reported[18] to result in reduction in lattice parameter by ~10% per mol of water molecules removed from the oxide structure.

The MCR (21.6) for the KCl solution is higher than the equivalent weight of H_3O^+, and the difference can be attributed to simultaneous insertion/extraction of K^+ accompanied by H_3O^+. This is also consistent with the XPS data, which shows the presence of K^+ within the oxide structure at the reduced state (Fig. 7c). The molar fraction of an alkali cation, X_M^+, within the inserting cation flux is estimated from the following equation

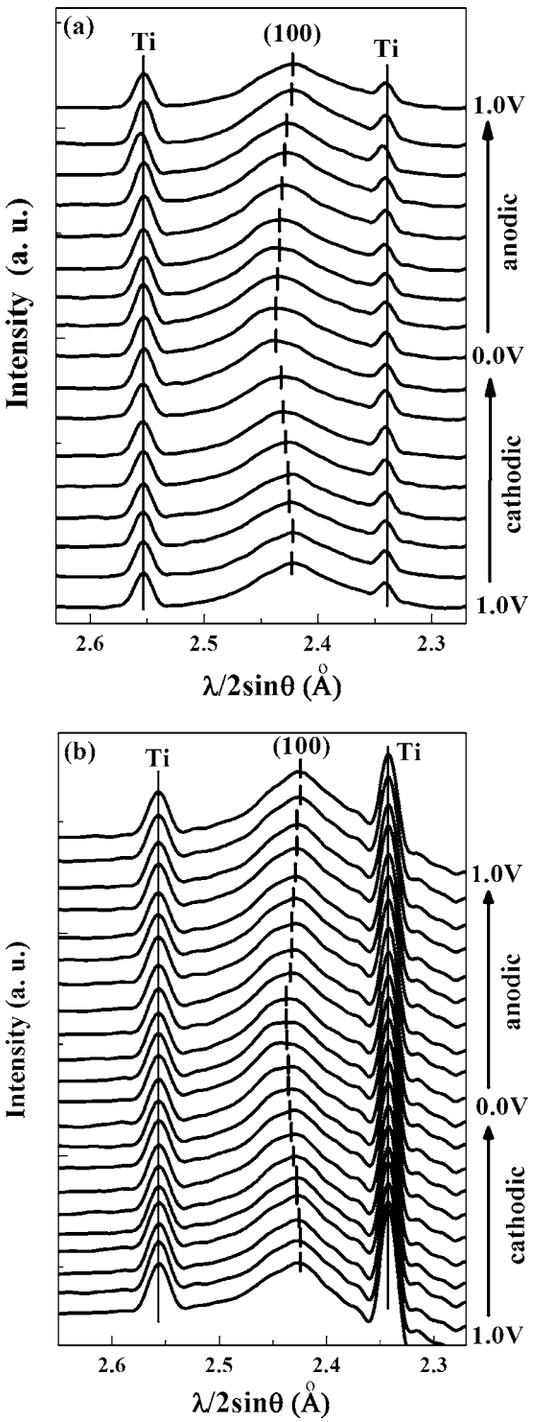

Figure 9. Synchrotron XRD patterns of $MnO_2{\cdot}nH_2O$ particle electrodes acquired in situ during CV cycling in (a) 1 M $NaCl_{(aq)}$ and (b) 1 M $KCl_{(aq)}$.

$$MCR = EW[H_3O^+] \times (1 - X_M^+) + EW[M^+] \times X_M^+ \qquad [6]$$

where *EW* is the equivalent weight of the species shown in the brackets, and M^+ represents alkali ion. The fraction for K^+ is determined to be 13.0%.

According to the rationale, Li^+ has a smaller equivalent weight than H_3O^+ and hence, the mixture flux of these two cations is expected to give a mean MCR in between their equivalent weights. This was indeed observed. This is also true for the case of Cs^+.

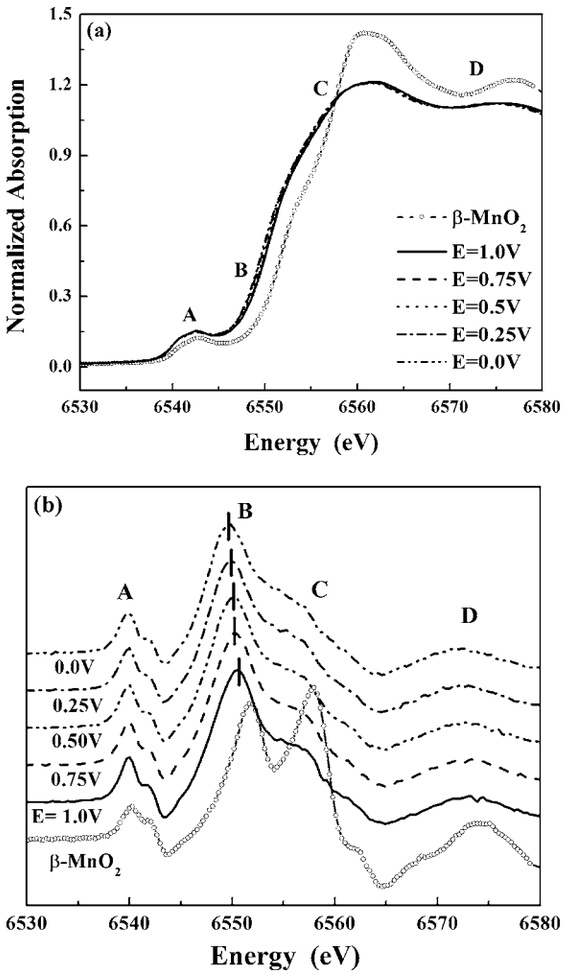

Figure 10. (a) XANES spectra and (b) their corresponding derivative curves taken in situ along the course of reduction in 1 M $KCl_{(aq)}$.

Accordingly, the contributions of these alkaline cations in the inserting flux are also calculated from Eq. 6, and they are listed in Table II. The XPS data did indicate that Ca^{+2} also inserted into the oxide lattice. The contribution from Ca^{+2}, however, cannot be determined from Eq. 6 because of the great similarity in equivalent weight between Ca^{+2} (20.0) and H_3O^+ (19.0).

As noted in Table II, for all the tested alkali-chloride solutions, H_3O^+ plays the predominant (>60%) role. The contribution from alkali ion first decreases and then increases with ionic size. To explain this trend, two energy factors are considered. First, the increase in free energy caused by lattice expansion would favor insertion of smaller cations. Second, the increase of free energy by removal of water molecules from the solvated cation would favor larger cations, which has a smaller charge density and hence, less solvated water molecules. The extent of insertion of either H_3O^+ or alkali cations would result from the balance between these two opposing factors. The lattice expansion factor may explain a decrease in insertion with increasing ionic size from Li^+ to Na^+. The dehydration factor may account for the subsequent increase in insertion with further increasing ionic size from Na^+ to Cs^+. The reaction schemes for insertion of H_3O^+ and concurrent process of alkali ion upon reduction can be expressed as

$$Mn(IV)O_2\cdot nH_2O + \delta e^- + \delta H_3O^+ \leftrightarrow (H_3O)_\delta[Mn(III)_\delta Mn(IV)_{1-\delta}]O_2\cdot nH_2O \quad [7]$$

The concurrent insertion of the alkali ion can be similarly expressed as

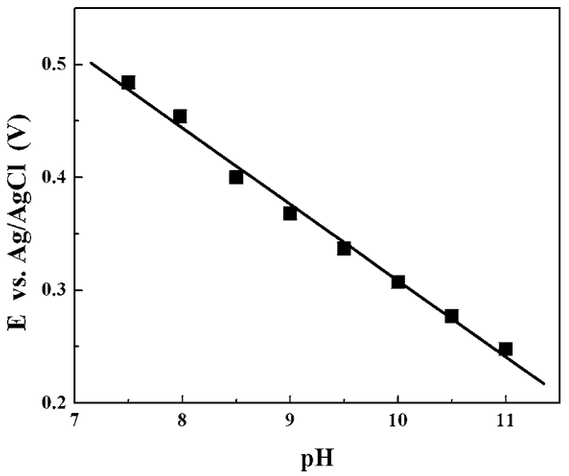

Figure 11. OCP of $MnO_2\cdot nH_2O$ thin-film electrode vs pH value in a 1 M NaCl solution.

$$Mn(IV)O_2\cdot nH_2O + \delta e^- + \delta M^+ \leftrightarrow M_\delta[Mn(III)_\delta Mn(IV)_{1-\delta}]O_2\cdot nH_2O \quad [8]$$

where M^+ is an alkali cation.

The open-circuit potential (OCP) of a thin-film electrode was measured as a function of pH value in a 1 M NaCl solution. The pH value of the solution was increased stepwise with an increment ΔpH of ~0.5, and the OCP was taken 30 min after the pH change. As shown in Fig. 11, the OCP-pH correlation gives a slope, dE/dpH, of −65.0 mV, which is very close to the theoretical value (−59.2 mV) for Reaction 7.

Finally, the present $MnO_2\cdot nH_2O$ films and particles possess the ε-MnO_2-type crystal structure. ε-MnO_2 has a space group of $P6_3/mmc$. Mn ions are located at 2*a* (0,0,0; 0,0,1/2) sites with half occupancy, and O at 2*c* (1/3,2/3,1/4; 2/3,1/3,3/4) sites. By orderly arranging the Mn ions at 2*a* sites between neighboring unit cells, one is able to generate superstructures corresponding to those of pyrolusite (β − MnO_2) and ramsdellite, along with other structures that possess tunnels parallel to edge-shared MnO_6 octahedron chains with rectangular- or square-shaped cross sections that are *n* octahedra by *m* octahedra on a side. The structures of the present $MnO_2\cdot nH_2O$ samples are likely the intergrowth of these superstructures, and the larger tunnels could easily accommodate the inserting cations and water molecules.[29]

Conclusions

The pseudocapacitive charge storage reactions of $MnO_2\cdot nH_2O$ in several alkali and alkaline salts solutions have been investigated mainly by EQCM, XPS, and synchrotron XRD. It has been established that charge transfer at the Mn sites upon reduction/oxidation is balanced by insertion/extraction of the solution cations into/from the oxide structure. H_3O^+ plays the predominant (>60%) role in all cases, and the extent of participation for alkali cations first decrease and then increases with ionic size.

Acknowledgment

This work was supported by the National Science Council of China under contract no. NSC 94-2214-E-002-003. The authors thank Dr. Jyh-Fu Lee and Din-Goa Liu at NSRRC for their assistance with XANES analysis.

National Taiwan University assisted in meeting the publication costs of this article.

References

1. B. E. Conway, *J. Electrochem. Soc.*, **138**, 1539 (1991).
2. S. Sarangapani, B. V. Tilak, and C.-P. Chen, *J. Electrochem. Soc.*, **143**, 3791 (1996).
3. D. C. Grahame, *Chem. Rev. (Washington, D.C.)*, **41**, 441 (1947).
4. M. A. V. DeVanathan and B. V. Tilak, *Chem. Rev. (Washington, D.C.)*, **65**, 635 (1965).
5. S. Trasatti and G. Buzzanca, *J. Electroanal. Chem. Interfacial Electrochem.*, **29**, 1 (1971).
6. L. D. Burke, O. J. Murphy, J. F. O'Neill, and S. Venkatesan, *J. Chem. Soc., Faraday Trans. 1*, **73**, 1659 (1977).
7. B. E. Conway, V. Birss, and J. Wojtowicz, *J. Power Sources*, **66**, 1 (1997).
8. J. P. Zheng and T. R. Jow, *J. Electrochem. Soc.*, **142**, L6 (1995).
9. T. R. Jow and J. P. Zheng, *J. Electrochem. Soc.*, **145**, 49 (1998).
10. H. Y. Lee and J. B. Goodenough, *J. Solid State Chem.*, **144**, 220 (1999).
11. H. Y. Lee and J. B. Goodenough, *J. Solid State Chem.*, **148**, 81 (1999).
12. N. L. Wu, Y. P. Lan, C. Y. Han, S. Y. Wang, and L. R. Shiue, in *Electrochemical Capacitor and Hybrid Power Sources*, R. J. Brodd, D. H. Doughty, J. H. Kim, M. Morita, K. Naoi, G. Nagasubramanian, and C. Nanjundiah, Editors, PV 2002-7, p. 95, The Electrochemical Society Proceedings Series, Pennington, NJ (2002).
13. N. L. Wu, S. Y. Wang, C. Y. Han, D. S. Wu, and L. R. Shiue, *J. Power Sources*, **113**, 173 (2003).
14. S. Y. Wang and N. L. Wu, *J. Appl. Electrochem.*, **33**, 345 (2003).
15. L. R. Shiue, N. L. Wu, D. S. Wu, C. W. Chao, and Y. P. Lan, U.S. Pat. 6,678,147 (2004).
16. J. P. Zheng, P. J. Cygan, and T. R. Jow, *J. Electrochem. Soc.*, **142**, 2699 (1995).
17. H. Y. Lee, V. Manivannan, and J. B. Goodenough, *C.R. Acad. Sci., Ser. IIc: Chim*, 565 (1999).
18. S.-C. Pang, M. A. Anderson, and T. W. Chapman, *J. Electrochem. Soc.*, **147**, 444 (2000).
19. M. Toupin, T. Brousse, and D. Bélanger, *Chem. Mater.*, **16**, 3184 (2004).
20. C. C. Hu and T. W. Tsou, *Electrochem. Commun.*, **4**, 105 (2002).
21. International Center for Diffraction Data (ICDD), File Card no. 89-5171.
22. Inorganic Crystal Structure Database (ICSD), File Data no. 78331.
23. M. C. Santos, A. J. Terezo, V. C. Fernards, E. C. Pereira, and L. O. S. Bullhões, *J. Solid State Electrochem.*, **9**, 91 (2005).
24. C. D. Wagner, W. M. Riggs, L. E. Davis, and J. F. Moulder, *Handbook of X-Ray Photoelectron Spectroscopy*, Physical Electronics, Perkin Elmer Corporation, Eden Prairie, MN (1995).
25. M. Toupin, T. Brousse, and D. Bélanger, *Chem. Mater.*, **14**, 3946 (2002).
26. M. Belli, A. Scafati, A. Bianconi, S. Mobilio, L. Palladino, A. Reate, and E. Burattini, *Solid State Commun.*, **35**, 355 (1980).
27. B. Ammundsen, D. J. Jones, and J. Roziere, *J. Solid State Chem.*, **141**, 294 (1998).
28. A. Ibarra-Palos, P. Strobel, O. Proux, J. L. Hazemann, M. Ann, and M. Morcrette, *Electrochim. Acta*, **47**, 3171 (2002).
29. J. E. Post, *Proc. Natl. Acad. Sci. U.S.A.*, **96**, 3447 (1999).